Soft Matter

Accepted Manuscript

Volume 1 | Number 1 | Jan 2013 | Pages 1–100

Soft Matter

www.rsc.org/softmatter

ROYAL SOCIETY
OF CHEMISTRY

www.rsc.org/softmatter

Soft Matter

ARTICLE

Experimental Observation of the Asymmetric Instability of Intermediate-Reduced-Volume Vesicles in Extensional Flow

Received 00th January 20xx,
Accepted 00th January 20xx

DOI: 10.1039/x0xx00000x

www.rsc.org/softmatter

Joanna B. Dahl,[a] Vivek Narsimhan,[b] Bernardo Gouveia, [a] Sanjay Kumar,[a,c] Eric S. G. Shaqfeh, [d,e] and Susan J. Muller [*a]

Vesicles provide an attractive model system to understand the deformation of living cells in response to mechanical forces. These simple, enclosed lipid bilayer membranes are suitable for complementary theoretical, numerical, and experimental analysis. A recent study [Narsimhan, Spann, Shaqfeh, *Journal of Fluid Mechanics*, 2014, **750**, 144] predicted that intermediate-aspect-ratio vesicles extend asymmetrically in extensional flow. Upon infinitesimal perturbation to the vesicle shape, the vesicle stretches into an asymmetric dumbbell with a cylindrical thread separating the two ends. While the symmetric stretching of high-aspect-ratio vesicles in extensional flow has been observed and characterized [Kantsler, Segre, Steinberg, *Physics Review Letters*, 2008, **101**, 048101] as well as recapitulated in numerical simulations by Narsimhan et al., experimental observation of the asymmetric stretching has not been reported. In this work, we present results from microfluidic cross-slot experiments observing this instability, along with careful characterization of the flow field, vesicle shape, and vesicle bending modulus. The onset of this shape transition depends on two non-dimensional parameters: reduced volume (a measure of vesicle asphericity) and capillary number (ratio of viscous to bending forces). We observed that every intermediate-reduced-volume vesicle that extends forms a dumbbell shape that is indeed asymmetric. For the subset of the intermediate-reduced-volume regime we could capture experimentally, we present an experimental phase diagram for asymmetric vesicle stretching that is consistent with the predictions of Narsimhan et al.

Introduction

Vesicles provide a valuable system to test our knowledge of the mechanical behavior of the lipid bilayer component of the cell membrane. Because of the structural complexity, heterogeneity, and complex functional properties of cell membranes and the cytoskeleton, it is extremely challenging to dissect how specific molecular components contribute to whole-cell mechanical properties based on studies with living cells. As a deformable membrane consisting of a phospholipid bilayer surrounding a liquid interior, vesicles lack the transmembrane proteins and dynamic cytoskeletal networks normally found in cells. Due to this simplicity, vesicles act as a reductionist model for cellular membranes that can be examined by complementary theoretical, numerical, and experimental approaches that would be difficult to perform on living cells.

The biophysics community has studied vesicles in linear flows in great detail theoretically[1-3] and computationally[4-10] and to a certain extent experimentally[11-19]. Due to the similarity to blood flow in the vasculature, vesicle behavior in shear flow (planar velocity field $\mathbf{v} = \dot{\gamma}(y\hat{\boldsymbol{x}})$ where $\dot{\gamma}$ is the shear rate and $\hat{\boldsymbol{x}}$ is the flow direction) has been a major area of investigation. Vesicles possess the characteristics of bending elasticity and constant surface area that capture some key aspects of red blood cell (RBC) dynamics in circulation.[‡] For example, experiments on individual vesicles reveal a range of motions (typically referred to as tumbling, tank-treading, and trembling) at transition points that depend on the shear rate and the viscosity ratio between the fluid interior and exterior to the vesicle[19,20]. These experimental observations agree reasonably well with numerical predictions[4,11,21] and furthermore recapitulate the tumbling, tank-treading, and trembling behavior observed for RBCs,[22,23] though agreement of vesicle and RBC dynamic behavior is not as good at low shear rates as at higher shear rates.[24] Vesicle models can also capture the intermittent swinging behavior of RBCs[22] if these models include membrane shear elasticity to represent the cell's cytoskeletal structure. [25]

---

[a] Department of Chemical and Biomolecular Engineering, University of California, Berkeley, Berkeley, CA, 94720-1460, USA. E-mail: muller2@berkeley.edu.
[b] Department of Chemical Engineering, Massachusetts Institute of Technology, Cambridge, MA, 02139, USA.
[c] Department of Bioengineering, University of California, Berkeley, Berkeley, CA, 94720-1762, USA.
[d] Department of Chemical Engineering, Department of Mechanical Engineering, Stanford University, Stanford, CA, 94305, USA.
[e] Institute of Computational and Mathematical Engineering, Stanford University, Stanford, CA, 94305, USA.

Electronic Supplementary Information (ESI) available: Electroformation protocol, justification to neglect gravity in bending modulus measurements, error analysis, vesicle shape measurement, cross-slot strain rate PIV measurement, and tables of plotted data. See DOI: 10.1039/x0xx00000x

In comparison to shear flow, vesicle behavior in extensional flow (planar velocity field $\mathbf{v} = \dot{\varepsilon}(x\hat{\mathbf{x}} - y\hat{\mathbf{y}})$ where $\dot{\varepsilon}$ is the rate of strain) has been much less studied. Extensional flow is the dominant flow type in regions with a rapidly changing cross sectional area normal to the flow direction, such as in the blood flow at transitions from larger to smaller blood vessels or in syringe needle injections. Experiments and numerical work have provided evidence that extensional fluid stresses are integral to hemolysis (instantaneous rupture of RBCs), and existing models for hemolysis that only account for simple shear stresses are insufficient.[26,27] Studying the deformation and stability of vesicles in extensional flow would improve our mechanistic understanding of cell damage within medical applications, such as RBC lysis in medical devices and artificial organs[27] and vesicle drug-delivery systems.[28,29] Within the area of vesicle dynamics research, the flow field around vesicles sedimenting under gravity is primarily elongational flow. The thin tether formed on settling vesicles observed experimentally[30] and recapitulated in numerical studies[31,32] looks similar to the vesicle shape instability studied here.

Steinberg and co-workers were among the first to perform experiments on vesicles in a planar extensional flow.[16,33] They considered very low reduced volume vesicles, where reduced volume is defined as the ratio of the vesicle's volume V to the volume of a sphere with the same surface area A: $\nu = 3V/4\pi a^3$ where $a = \sqrt{A/4\pi}$ is the vesicle's effective radius based on surface area. For a perfectly spherical vesicle, $\nu = 1$, and the vesicle has no excess area to deform its shape when subjected to fluid stresses. For $\nu < 1$, the vesicle is non-spherical and has excess area to deform. For their very low reduced volume vesicles, Steinberg and co-workers observed that the vesicle extension saturates at a steady value below a critical extension rate. However, above a critical extension rate, these long, tubular vesicles undergo a shape transition from tubular to dumbbell shaped. The central tube connecting the two ends of the dumbbell extends linearly with the strain until it undergoes a pearling instability.[16]

Recently, a stability boundary has been predicted for vesicles in extensional flow as a function of reduced volume and capillary number[34] (i.e., ratio of bending to viscous forces: $Ca = \mu\dot{\varepsilon}a^3/\kappa$, where μ is the viscosity of the fluid surrounding the vesicle and κ is the membrane's bending modulus). In extensional flow, vesicles with $\nu > 0.75$ will deform into a prolate ellipsoid and remain stable. Low reduced-volume vesicles ($\nu < 0.56$) will deform into a symmetric dumbbell and above a critical extension rate, extend without bound in a manner similar to capillary breakup of droplets. In the intermediate reduced volume regime ($0.56 \leq \nu < 0.75$), vesicles in elongational flow are predicted to stretch into an asymmetric dumbbell shape as a result of destabilizing curvature changes of the membrane, similar to the Rayleigh-Plateau phenomenon. While Steinberg and co-workers have experimentally explored the stability of low-reduced-volume vesicles in planar extensional flow[16], only one of their observations (the case $L_0/D_0 \sim 4.2$, which corresponds to $\nu\sim 0.62$) occurs in the intermediate-reduced-volume regime of interest to the present study. Thus while the critical dynamics of low-reduced-volume, tubular vesicles in extensional flow have been explored experimentally, observation of the asymmetric dumbbell instability of intermediate-reduced-volume vesicles has not been reported.

In this paper, we present an experimental study of intermediate-reduced-volume vesicles in extensional flow and compare our results to the predictions of Ref. 34. First we describe our strategies to produce intermediate-reduced-volume vesicles. Next we discuss the microfluidic cross-slot devices that generate planar extensional flow and confirm this flow field with particle image velocimetry (PIV) measurements. We then describe our procedure for measuring the bending modulus of the vesicles from analysis of membrane thermal fluctuations. Finally, we present the experimental stability diagram and compare it to the predicted stability boundary.

Experimental Methods and Materials

Vesicle Preparation. Vesicles are prepared from a mixture of 1,2-dioleoyl-*sn*-glycero-3-phosphocholine (DOPC, Avanti Lipids) with fluorescent 1-oleoyl-2-{6-[(7-nitro-2-1,3-benzoxadiazol-4-yl)amino]hexanoyl}-*sn*-glycero-3-phosphocholine (NBD PC, ex/em 460/534 nm, Avanti Lipids). Unilamellar vesicles were prepared using the electroformation method.[35] Because the fluorescent NBD group on the NBD PC tends to flip up into the molecule's head-group region at room temperature and disrupt the lipid bilayer membrane,[36] we use high concentrations of NBD PC in order to promote the formation of floppy, intermediate-reduced-volume vesicles we wish to study. DOPC (1.68 mg/mL) and NBD PC (0.32 mg/mL) were mixed with chloroform for a total lipid concentration of 2 mg/mL. This recipe is similar to that in Ref. 16. We found that above 3 mg/mL total lipid concentration, most vesicles were spherical even with high amounts of NBD PC. Vesicles were formed in 0.1 M sucrose (Sigma). More details of the electroformation procedure are available in the supporting information. Vesicles are handled gently by using large diameter needles and pipettes of inner diameters larger than 0.8 mm (18 gauge and lower). To further promote the production of floppy vesicles, we added a small amount of 0.2 M sucrose to the vesicle suspension to achieve a +2 mOsm difference between the interior and the exterior of the vesicle, which has the effect of driving water out of the vesicle interior until the sugar concentrations are equal on either side of the membrane. This combination of gentle osmotic deflation with 15.8 mol% NBD PC concentration tended to produce lower reduced volume vesicles, though vesicles with reduced volumes $\boldsymbol{\nu} < \mathbf{0.75}$ are still quite rare. Typical reduced volumes are $\boldsymbol{\nu} \sim \mathbf{0.8}$ compared to $\boldsymbol{\nu} \sim \mathbf{0.9}$ vesicles with 15.8 mol% NBD PC and no osmotic deflation and $\boldsymbol{\nu} \sim \mathbf{0.95}$ with lower concentration of NBD PC and no osmotic deflation, as measured during trapping in the cross-slot (see below).

Fluorescence Microscopy. Fluorescence microscopy on an inverted microscope is used to image vesicles in microfluidic cross-slot devices and for thermal fluctuation bending modulus measurements under quiescent conditions. A Leica DMIRE2 inverted microscope is equipped with a dual-band excitation/emission filter (Chroma 51004v2, 460-500/510-560 nm), permitting the excitation of, and emission capture for, the NBD groups from the external light source (Leica EL6000). The microscope stage has a digital readout to micron resolution so that the height of vesicles above the device glass bottom can be estimated. The internal mechanical shutter in the light source, controlled by a function generator (25 Hz square wave, 50% duty cycle), is utilized in order to reduce the amount of illumination to the vesicles and to reduce photobleaching. No coordination between the light source shutter and the camera is necessary because vesicles are visible in every frame with an amount of flickering that does not affect edge detection. The objectives used are 10x (Olympus, 0.754 pixel/µm) and 20x (Leica, 1.25 pixel/µm) for PIV measurements, water-immersion 63x (3.93 pixel/µm) for cross-slot measurements, and oil-immersion 100x (6.36 pixel/µm) for thermal fluctuation bending modulus measurements. Images are captured with a monochromatic Photometrics Cascade 512b CCD camera (512x512 pixels). Movies are captured at a rate of 27-28 fps with an exposure time of 1 ms. Images are analysed with in-house software in ImageJ (NIH) and Matlab (2013v, MathWorks). More details of edge detection are given below. Additionally, we used fluorescence confocal microscopy (Nikon Eclipse Ti, Andor CSU-x1 spinning disk confocal) with a 60x oil-immersion objective (11.057 pixel/µm) to perform three of the thermal fluctuation bending modulus experiments reported. For those three measurements, movies were captured with a Zyla 4.2 PLUS sCMOS camera at 5 ms exposure and approximately 100 fps.

Microfluidic Cross-slot and Velocity Field Measurements. Microfluidic cross-slots are fabricated using standard soft-lithography (Figure 1). This geometry, consisting of two channels that intersect at ninety degrees, is a convenient platform for generating a planar elongational flow. Masters were made from SU-8 on silicon wafers or through the use of a dry film photoresist on stainless steel wafers. To achieve very deep devices, five layers of 75-µm thick dry film photoresist was laminated onto a steel wafer and developed (Riston GoldMaster GM130 photoresist, DuPont). The cross-slot channel widths are 2 mm (x and y directions, *cf.* Figure 1), and the channel depths (z direction) are 150, 158, and 383 µm, as measured by a profilometer measurement of the SU-8 master or PDMS device for those made from the Riston masters. Fluid from the two opposing inlet channels impinges at the center of the cross-slot device, creating a hyperbolic flow field that we verify using micro-PIV (see next paragraph). The image plane for all our measurements is the center of the channel in the z direction. The centerplane of the device was found by taking the average height of the top and bottom of the device, located by focusing on stationary particles adhered to those surfaces.

To determine the rate-of-extension near the stagnation point of the fluid, we perform micro-PIV[37,38] on a neutrally-buoyant suspension of 0.005% v/v 1 µm fluorescent polystyrene spheres (FluoSpheres, ex/em 540/560 nm, Molecular Probes) in a 0.367 M sucrose solution (Sigma) for the 158- and 383-µm deep cross-slots. To prevent particle aggregation, we also add Tween-20 (Sigma-Aldrich) to the suspension. We flow the suspension into the device at flow rates between 100-500 µL/hr and image the spheres near the stagnation point using a 10x objective. We calculate the velocity field by using an open-source PIV software (PIVlab v1.32[39]) with our own customizations, described below. The instantaneous displacement vector at each point is determined by cross-correlating the fluorescence intensity profile between small interrogation regions in two images separated in time by some Δt. The instantaneous velocity is then obtained by dividing the displacement by the time interval between the images. The average velocity vector for a given flow rate is determined from the average cross-correlation function of each interrogation area. The pair-wise correlation matrices are evaluated in the frequency domain, and the peak locations of the average cross-correlation functions are refined with subpixel precision using a 2D Gaussian function (3x3 neighborhood fit). We sample interrogation areas of 20 x 20 pixels with 50% overlap and use 500 frames in a typical movie. Images are subjected to contrast limited adaptive histogram equalization before cross-correlation to improve the velocity measurement quality. Velocity vectors are validated with the normalized median check[40] to filter outliers, and missing vectors are replaced with values interpolated from nearest neighbors. Due to limited PIV data, we estimate the extensional shear rate in the 150-µm deep device by performing PIV analysis on concentrated vesicle suspensions.

Our experimental PIV measurements indicate that within the camera field of view at 10x, which corresponds to approximately 600 x 600 µm^2 (Figure 2(a)), the flow generated by the cross-slot is practically planar extensional flow, i.e., $\mathbf{v} = \dot{\varepsilon}(x\hat{\mathbf{x}} - y\hat{\mathbf{y}})$, where $(0,0)$ is the stagnation point, x is the axis along the outlet direction, and y is the axis of the inlet. We confirmed that the velocity magnitude $|\mathbf{v}|$ is radially symmetric and varies linearly with the distance from the stagnation point as $|\mathbf{v}| = \dot{\varepsilon}r$ (Figure 2(b)). The measured extension rates as a function of the inlet flow rate compare well to the predicted $\dot{\varepsilon}$ from Hele-Shaw flow (Figure 2(c)). Our excellent agreement with the Hele-Shaw predictions shows that the extension rate is within 5% of the stagnation point value for the entire viewing window at 63x (409 x 409 µm). A linear fit of $\dot{\varepsilon}$ vs. flow rate allows for interpolation and extrapolation of $\dot{\varepsilon}$ at other flow rates used in the cross-slot for vesicle stretching. The uncertainty in $\dot{\varepsilon}$ was determined as the standard deviation of the squared residuals to the linear fit (for additional details, see the Electronic Supplementary Information).

Bending Modulus Measurement

Imaging vesicles. We imaged vesicles in a CoverWell perfusion chamber (CoverWell 9 mm diameter, 0.5 mm deep perfusion chamber gasket, Invitrogen, Molecular Probes) using the 100x objective for maximum resolution for the Leica system and 60x for the confocal microscopy system. The chamber ports are sealed with tape to reduce evaporation and therefore convection within the CoverWell so that the vesicles in the well were sufficiently still, only moving tens of microns during the 45 to 90-second movie capture. For the measurements performed with confocal microscopy, vesicles were made to sediment by diluting 1:1 with 0.1 M glucose solution. The gravitational effect is sufficiently small to not affect the bending modulus analysis according to the criteria specified in Ref. 41 (see Electronic Supplementary Information). Vesicles suitable for bending modulus measurement were isolated from their neighbors, sufficiently far away (at least two vesicle diameters) so that the thermal fluctuations of the vesicle of interest were not hindered. For neutrally buoyant vesicles, we only used vesicles that were at least one diameter above the glass slide. Vesicle contours must also be free of large defects, usually in the form of visible bright clumps of lipids. Electroformation does not exclusively produce unilamellar vesicles; some vesicles have a brighter contour under fluorescence illumination than others, indicating that the membrane is likely multilamellar. Thus we consider vesicles that have the least bright, smooth membrane and assume they are unilamellar.

Movie capture considerations. In order to span the phase space of the vesicle, the bending modulus measurement movies must have both enough frames to provide sufficient representation of available configurations and have a long enough duration so that the lower order modes with longer relaxation times are resolved. We consider a movie duration that is at least three times the longest modal relaxation time to be of sufficient length, at which point the slowest exponentially decaying mode will have relaxed to $e^{-3} \sim 4\%$ of its original amplitude. Thermal fluctuation amplitudes had to be large enough to be able to be resolved above the experimental noise of edge detection (~1 pixel), which typically means amplitudes greater than 2 pixels are sufficient. Depending on the camera specifications, fluctuations visible by eye are not necessarily large enough to yield good edge detection and analysis. Within a gently osmotically deflated batch, the number of vesicles with unilamellar, defect-free, large amplitude fluctuations is quite small. We typically find only 10-20 unilamellar vesicles in a CoverWell sample with large fluctuations that are candidates for bending modulus measurement analysis, and only 2-8 of these vesicles yield high quality bending modulus measurements that pass all the requirements described below in the analysis procedure.

Analysis procedure. We use the general procedure outlined by Méléard et al.[42] that provides a statistical approach to measure bending modulus with quantitative selection criteria to exclude vesicles that do not conform to the quasi-spherical theory. We detect the vesicle membrane contour in each movie frame by finding the location of the maximum gradient of the intensity along rays drawn at 1° intervals from the contour center of mass. We achieve sub-pixel edge detection resolution by defining the vesicle contour location as the maximum of a parabola fit to the 5-point neighborhood around the ray maximum gradient location. Spurious contour points that are more than two pixels away from its two nearest neighbors or more than 4 standard deviations away from the mean radius value are discarded. For the detected vesicle contour, we calculate the angular correlation function:

$$\xi(\phi,t)=\frac{1}{2\pi R^2}\int_0^{2\pi}\Delta\rho(\theta+\phi,t)\Delta\rho(\theta,t)d\theta \tag{1}$$

where $\Delta\rho$ is the experimentally-measured deviation of the vesicle radius from its mean value at the point in time t: $\Delta\rho(\theta,t)=\rho(\theta,t)-\frac{1}{2\pi}\int_0^{2\pi}\rho(\theta,t)d\theta.$ R is the average radius of the vesicle over all time. Assuming the vesicle is quasi-spherical with constant area and volume, the Fourier modes of the correlation function are exponentially distributed with a mean that depends on two parameters: the reduced bending modulus $\bar{\kappa}=\kappa/kT$, where k is the Boltzmann constant and T is temperature, and reduced surface tension $\bar{\sigma}=\sigma R^2/\kappa$.[42]

$$\xi(\phi,t)=\sum_{m=2}^{\infty}\chi_m\cos(m\phi) \tag{2}$$

$$<\chi_m>=\sum_{n\geq m}^{\infty}\frac{2(\Theta_n^m)^2}{\bar{\kappa}(n+2)(n-1)[\bar{\sigma}+n(n+1)]} \tag{3}$$

In the above Equation (3), Θ_n^m are the normalized, associated Legendre polynomials[§] evaluated at $\cos(\theta)=1$. See Ref. 42 for derivations. To determine the bending modulus, we perform the following:

1. At each instance of time, we measure the Fourier modes of the angular correlation function $\xi(\phi,t)$ (i.e., Equation (1)). We examine modes $m = 2-30$.
2. We check if modes are exponentially distributed by performing a Kolmogorov-Smirnoff test.[43] For the modes that pass this test, we calculate their average amplitude $\bar{\chi}_m$ over all time to obtain experimental measurements of the modal exponential distribution rate parameters and perform a two-parameter fit to the theoretical values $<\chi_m>$ from Equation (3) to get estimates of the bending modulus and surface tension $(\bar{\kappa},\bar{\sigma})$. The merit function we optimize is:

$$E=\sum_{m=m_{min}}^{m_{max}}\frac{(<\chi_m>-\bar{\chi}_m)^2}{\bar{s}_m^2} \tag{4}$$

where $\bar{s}_m$ is the measured standard deviation of each Fourier mode and m_{min} and m_{max} are the smallest and largest Fourier mode numbers included in the analysis. The choices of m_{min} and m_{max} for which $\bar{\kappa}$ and $\bar{\sigma}$ are the most uncorrelated (i.e., Cor($\bar{\kappa}$,$\bar{\sigma}$) closest to zero) are considered to yield the final answers for $\bar{\kappa}$ and $\bar{\sigma}$.

To gather estimates for the variance of $\bar{\kappa}$ and $\bar{\sigma}$ for a single vesicle, we bootstrap the experimental data—i.e., we re-measure the bending modulus $\bar{\kappa}$ and the surface tension $\bar{\sigma}$ by randomly resampling the experimental Fourier modes χ_m with replacement. This procedure yields confidence intervals for $\bar{\kappa}$ and $\bar{\sigma}$ as well as their correlation coefficient Cor($\bar{\kappa}$,$\bar{\sigma}$). If the bending modulus and surface tension are too correlated (i.e., $\mathrm{Cor}(\bar{\kappa},\bar{\sigma}) < -0.85$), we exclude the vesicle from analysis as the statistics are poor. Furthermore, we only consider vesicles with a positive surface tension. After determining the bending modulus, we calculate the bending time scale of each mode.[44]

$$\tau_m = \frac{\mu R^3}{kT\bar{\kappa}} \frac{(2m+1)(2m^2+2m-1)}{m(m+1)(m+2)(m-1)[\bar{\sigma}+m(m+1)]} \qquad (5)$$

If the bending time scale of any mode is longer than the camera exposure time (1 or 5 ms) or the movie duration is shorter than three times the longest modal bending time scale, we repeat steps 1-2 again while excluding these modes. We correct for the integration time of the camera as detailed in Faucon et al.[45] The $\bar{\kappa}$ value and uncertainty used to determine the capillary number for plotting in the stability diagram is taken to be the sample mean and standard error of the mean of six individual measurements.

For the bending modulus measurements, we analyze frames in which the perimeter and area of the vesicle vary by less than 5 percent of the median value of the movie, as the assumption of constant area and volume are crucial for the validity of the above equations. We also make sure to choose vesicles with membrane fluctuations that are above the threshold noise of edge detection (i.e., > 1 pixel). Lastly, we only consider quasi-spherical vesicles in this analysis. The vesicles we examine in a cross-slot later in this paper are far from this quasi-spherical limit, but we will assume that the bending moduli we gather here will be representative of the entire batch of vesicles, regardless of their initial shape configuration.

Vesicle Elongation in Extensional Flow

Vesicles flowing in one or both inlets are elongated at constant strain rate in the extensional flow of the cross-slot and observed at the centerplane with the 20x or 63x objective, (Figure 1). Matched density of the inner and outer fluids is important for observing vesicles at the stagnation point for tens of seconds in the center of the z plane. By adjusting the height difference between the two outlet reservoirs and therefore adjusting the relative pressure between the two outlets, vesicles can be brought to and trapped at the stagnation point location and observed up to and beyond the maximum movie length of 90 seconds. Due to small perturbations in the system (e.g. reservoirs open to room pressure fluctuations), the vesicle trapping is not stable, and minor adjustments to the outlet pressure difference are needed to maintain the vesicle position near the stagnation point.

Vesicles are observed for 7-90 seconds at the stagnation point region to determine their stability or instability in extensional flow. Good vesicle candidates are unilamellar as judged by relative brightness, have no interference from neighboring vesicles, and are defect-free so that the membrane surface area and volume remain constant. A measure of shape before instability must be possible in order to include the vesicle on the stability diagram. For sufficiently spherical vesicles ($\nu \geq 0.8$), vesicle contour location is defined to sub-pixel resolution as the location of the maximum intensity gradient along rays drawn from the contour center of mass, using the same edge detection method used for the bending modulus measurements. The contour of less spherical vesicles ($\nu < 0.8$), for which drawing rays from the center of mass yields unevenly spaced contour points, is detected using the Sobel operator that approximates the gradient of the image intensity. To calculate the vesicle's reduced volume, the surface area and volume of the vesicle are estimated by revolving the observed 2D shape about the vesicle's long axis (more details in the Electronic Supplementary Information). The volume and surface area calculated from the left and right halves of the vesicle are found separately by numerical integration of a cubic spline fit, and the vesicle surface area and volume for a movie frame is the average value with uncertainty taken to be one half the discrepancy between the left and right halves. The final vesicle reduced volume is evaluated from the mean of the frame surface areas and volumes weighted by the individual uncertainties. As many movie frames as possible are used to determine the vesicle shape, with as few as 8 frames for one unstable vesicle and up to 200+ frames for most stable vesicles.

Results

Bending Modulus Measurements

We found that high levels of NBD PC dye (15.8 mol%) in our vesicle membranes lead to a bending modulus of $(14.94 \pm 0.40) \cdot kT$ (Figure 3). The bending modulus measurements have relatively small uncertainties and high precision, even though individual measurements were performed on two different microscopy systems and on batches of vesicles prepared on different days.

Vesicle Observations and Measurements in Extensional Flow

Vesicles experience a uniform extension rate as they become trapped in the stagnation region of the flow (Figure 2). In this region, the vesicle deformation reaches steady state (Supplemental Movie 1) or in a few instances, the vesicle stretches asymmetrically (Supplemental Movie 2). Every observed vesicle instability was indeed asymmetric; images from independent observations of the shape instability at short times are shown in Figure 4. The temporal evolution of the dumbbell shape and its stretching after several seconds of trapping at the stagnation point is shown in Figure 5. Once the instability occurs, the central tube in the vesicle elongates until the ends are out of the field of view. The bulbous ends become increasingly spherical during this stretching process as well. Furthermore, beads or pearls form on the tube in all cases in which asymmetric dumbbells were observed, including vesicles excluded from the stability diagram for reasons discussed below.

Some vesicles undergo the asymmetric instability but are excluded from the stability diagram for one or more of the following reasons: (A) a lack of movie frames from which to measure the pre-instability vesicle shape due to obstruction by other vesicles or being out-of-focus, (B) transient passing of the vesicle through the stagnation point region without extended trapping at the stagnation point location, (C) possible interference by a neighboring vesicle, and (D) termination of movie capture before the full instability evolution due to reaching the limit of on-board camera memory. Brighter multilamellar vesicles or those that possess visible defects are common, and these are excluded because their membrane properties would be different than defect-free unilamellar vesicles. Often these types of vesicles gradually collapse to a sphere as lipids from the membrane bud off into the vesicle interior or exterior.

Our experimental diagram includes a range of stable and unstable points that agree with the theoretical predictions (Figure 6). We break the unstable data points into two groups. The squares represent unstable vesicles for which we obtained sufficient images at short times to assign the reduced volume with confidence. The triangles represent unstable vesicles for which we have greater uncertainty in the reduced volume as this quantity was estimated from one still image at short times (see Figure 4(b) and (c) for snapshots). The error bars for all unstable vesicles are dominated by uncertainty in reduced volume due to a limited number of frames that could be analyzed before the onset of asymmetric instability. All other uncertainties are smaller and hence not included in the graph. See Table S2 in the Electronic Supplementary Information for a full list of data points as well as their uncertainties.

Discussion

Bending Modulus

A high concentration of NBD PC perturbs the lipid bilayer in ways that could increase or decrease the membrane elastic bending modulus. For example, excitation of lipid fluorophores can produce peroxides that cause the enlargement of liquid-ordered phase regions and hence a stiffer membrane.[46] Just 2 mol% NBD PC added to POPC (1-palmitoyl-2-oleoyl-*sn*-glycero-3-phosphocholine) vesicles resulted in a larger bending modulus with a broader distribution relative to the mean, the latter effect most likely arising from varying degrees of light-induced peroxide content.[47] A membrane softening effect can also arise from the looping up of the acyl-chain-labeled NBD fluorescent group from the interior of the bilayer into the membrane interface due to its polarity. Above the lipid transition temperature, NDB groups completely loop up due to favorable hydrogen bonding with the lipid head group or interfacial water molecules.[36] The looping up of NBD groups increases the NBD PC molecule headgroup area compared to unlabeled molecules, and was estimated to cause a 3% increase in cross-sectional area per fluorescently labeled POPC molecule.[48] At room temperature of 23˚C, the vesicles in our experiments are certainly in the fluid phase (transition temperature of DOPC is -17˚C). This phenomenon could result in a softening effect similar to the presence of peptide inclusions in the bilayer. For instance, the bending modulus of DOPC vesicles decreases 40% when 2 mol% of a synthetic fusion peptide FP23 is incorporated into the membrane.[49] POPC vesicles are softened with the inclusion of magainin, a peptide that adsorbs to the outer lipid layer as a α -helix lying parallel to the bilayer, which the authors interpreted using a continuum model as forming local, mobile high-curvature regions in the membrane.[50] Given the modest scatter in bending modulus between individual vesicles and the qualitative observations of softening with increased NBD concentration, we presume the “looping up” effect was slightly more dominant than the peroxidation effect for our system.

Our measurements of 15.8 mol% NBD PC/DOPC vesicles are in the same range as reported measurements of pure DOPC vesicles in similar experimental conditions, so the competing effects of NBD probes in the bilayer may overall have a moderate effect on membrane properties. At similar temperature and sugar concentrations to our measurements (25˚C, 0.1 M sucrose interior solution, 0.11 M glucose exterior to enhance contour contrast), researchers measured a bending modulus of $(11.7 \pm 1.5) \cdot kT$ for pure DOPC vesicles using micropipette aspiration.[49] Bending modulus measurements from thermal fluctuation analyses are typically higher compared to micropipette aspiration measurements,[51,52] thus our higher κ measurement could be due to the difference in methods as well as vesicle lipid composition. From thermal fluctuation measurements of pure DOPC vesicles in lower sugar concentration (0.01 M glucose), Gracia et al. reported $\kappa = (26.4 \pm 2.4) \cdot kT$.[53] Two studies utilizing both thermal fluctuation analysis and micropipette aspiration indicate that vesicle bending modulus decreases with increasing sugar concentration in the surrounding aqueous phase[49,54], possibly due to the vesicle uptake of sugars from the surrounding aqueous solution.[55] For DOPC vesicles, increasing the sugar concentration from 0.008 M sucrose/glucose (interior/exterior) to 0.1 M sucrose/0.11M glucose decreased the bending modulus by a factor of almost two, as measured by micropipette aspiration.[49] So if thermal fluctuation measurements scale similar to micropipette aspirations, $\kappa = 26.4 \cdot kT$ in 0.01 M sugar would decrease to $\sim 13.2 \cdot kT$ in

0.1 M sugar, close to our measured values. However, recent low angle X-ray measurements do not support such a bending modulus dependency on sugar concentration.[56] Rather, these researchers found no significant change in bending modulus for DOPC vesicles in sucrose or glucose solutions ranging from 0.1 M to 0.45 M sugar concentrations. Thus the value of bending modulus for simple lipid bilayers remains an unsettled issue. Our measurements not only characterize the vesicle system for this study but also provide more experimental data for DOPC vesicles to the field of lipid physics, albeit with a high concentration of fluorophores incorporated into the membrane.

The rigorous statistical tests and criteria we employed eliminated most vesicles from consideration. The smaller sample population scatter we achieved is consistent with other implementations of this more rigorous statistical approach, which has been shown to increase the precision of bending modulus measurements compared to average-based methods in a direct comparison.[42] Average-based methods rely on the user to visually check if the vesicle meets the theory requirements (quasi-spherical, defect-free, freely fluctuating). Based on our experience, this method typically leads to fairly large scatter in vesicle bending modulus measurements because vesicles that fail theory requirements are not always identifiable from a visual check of the thermal fluctuations. The statistical method of Méléard et al.[42] that we employed uses the full Fourier amplitude spectra of the contour autocorrelation function that adhere to the underlying theory (i.e. pass the Kolmogorov-Smirnoff test). Due to this and other quantitative checks detailed in the Methods Section, we are able to identify and discard vesicles that give reasonable but more scattered answers. For instance, vesicles that looked quasi-spherical and defect-free, but upon analysis yielded highly correlated bending modulus and surface tension values and were therefore discarded, resulted in both larger and smaller measurements, e.g. $(7.18 \pm 0.22) \cdot kT$ and $(28.72 \pm 1.73) \cdot kT$.

Vesicle Asymmetric Instability

In this paper, we present the first experimental observations of the asymmetric instability of vesicles in extensional flow. Although we were not able to guarantee that the vesicle remained exactly with its center of mass at the stagnation point, we can reasonably assume the asymmetric dumbbell formation we observed was indeed the predicted instability and not a result of the vesicle experiencing an asymmetric flow field. First, the cross-slot device produces quite uniform extensional strain rate $\dot{\varepsilon}$ throughout the entire observation window. Within the field of views in which we observed vesicles in extensional flow—(410 μm)^2 at 20x and (130 μm)^2 at 63x—our PIV measurements provide evidence of uniform extension rate. Furthermore, 3D COMSOL simulations show $\dot{\varepsilon}$ varies by less than 5% over these observation windows for the smallest cross-slot dimensions. Second, the time spent in the observation window (7-90 seconds) is comparable to or longer than the time scale of the instability. If the trapped time is larger or comparable to the inverse of the growth rate predicted from linear stability analysis, then we can assume the vesicle was sufficiently trapped during the instability process. For instance, the growth rate of the instability at $\nu = 0.65, Ca = 100$ is approximately $0.3 \cdot \dot{\varepsilon}$.[34,57] If the strain rate is 0.4 s^{-1}, then the time scale of the instability is approximately 8 seconds.

Due to the difficulty in reliably generating intermediate reduced volume vesicles via electroformation, vesicles that became unstable in the cross-slot were a rare event, so it was difficult to investigate the entire (ν, Ca) space. However, the measured points are consistent with the numerical predictions.[34,57] In particular, the stable point $(\nu, Ca) = (0.702, 6.83)$ is at an intermediate reduced volume that could have become unstable at a slightly higher capillary number (Supplemental Movie S3). Though admittedly, for such close proximity to the stability boundary we would have to trap the vesicle for a very long time to observe the instability if it were to occur, and we only trapped the vesicle for 19.8 seconds at a strain rate of $\dot{\varepsilon} = 0.368$ s^{-1}. However, this is still longer than the inverse of the predicted growth rate of the instability, estimated from linear stability analysis of $\nu = 0.65$ at $Ca \sim 8$ to be $\sim 1/(0.2 \cdot \dot{\varepsilon}) = 13.6$ seconds.[34,57] All other data points are well within the appropriate stable and unstable regimes. Furthermore, every vesicle that became unstable did so asymmetrically, corroborating evidence that the proposed physical mechanism of destabilizing membrane curvature changes is the cause of this instability.[34]

Without performing detailed studies, we point out a few observations. Pearling of vesicles has been studied experimentally [58-60] and theoretically.[61-63] Interestingly, recent theory for pearling suggests that pearling only occurs for reduced volumes $\nu < 0.6$.[64] We observed pearling of every tether following asymmetric dumbbell formation, including vesicles with $\nu > 0.6$, once the tether reached a certain length. Possibly there are important factors not considered in the modeling work, such as membrane thermal fluctuations. Also, all the unstable vesicles we included in the stability diagram are close to the vesicle aspect ratio below which Kantsler et al.[16] did not observe a stretching transition for high-aspect-ratio, tubular vesicles in extensional flow. Assuming a cylindrical geometry with an initial aspect ratio L_0/D_0, the authors reported no observations of tubular vesicle to dumbbell transitions for $L_0/D_0 < 4.2$ where the critical strain rate for their tube to dumbbell transition diverges. Approximating the aspect ratio of our reported unstable vesicles by taking the ratio of its length to average width, the aspect ratios are roughly $3.8 - 6.3$. Thus our observations of instability are consistent with Kantsler et al. Those authors also observed tubular vesicles to form seemingly symmetric dumbbells at an initial critical strain rate and then experience a secondary pearling instability at a higher critical strain rate. In contrast, we always observed pearling of the tether following the initial shape instability.

Conclusions

A droplet with a complex membrane experiences very different flow dynamics than one with a standard fluid-fluid interface. We present an example of this statement by trapping a vesicle in extensional flow and visualizing an asymmetric shape instability that has not been seen for clean droplets. This phenomenon arises from the near incompressibility of the lipid bilayer. In the future, it will be interesting to see if other cell-like objects with different interfacial behavior will exhibit the same phenomenon. One example that may show promise is a microcapsule with a membrane made of a stiff, highly crosslinked polymer.[65-67] We note that the vesicles examined in this work all stretched indefinitely when the instability occurred. Presumably, these vesicles will eventually break up. Thus, in some sense, we have experimentally determined conditions under which these entities will eventually fail by extensional flow, which would be important for various applications such as drug delivery, blood flow in artificial organs, or any biomedical applications in which suspended cells experience a sudden change in the channel diameter.

Acknowledgements

This material is based upon work supported by the National Science Foundation Postdoctoral Research Fellowship in Biology under Grant No. 1308051 to J.B.D. V.N. received support from the Stanford Liebermann Fellowship. This work was supported by additional grants from the National Science Foundation (1105539 to S.K., 1066334 to S.J.M. and E.S.G.S). S.K. received support from the National Institutes of Health (IMAT R21CA174573). We would like to thank M. Bakalar and D. Fletcher from Bioengineering at UC Berkeley for the use of the confocal microscope for some of the bending modulus measurements.

Notes and references

‡ We would not expect the vesicle to completely recapitulate all red blood cell flow behavior because the red blood cell (RBC) membrane is more complicated than a pure lipid bilayer. Most notably, the RBC possesses a cytoskeleton that provides the cells with resistance to shearing forces, unlike fluid phase vesicles that have practically zero elastic shear modulus.

§ The associated Legendre polynomials are the angular part of the spherical harmonics: $Y_n^m(\theta,\phi) = \Theta_n^m(\cos\theta)\exp(im\phi)$. We normalize $\Theta_n^m(\cos\theta)$ so that the spherical harmonics are orthonormal: $\langle Y_n^m, Y_{n'}^{m'}\rangle = \delta_{nn'}\delta_{mm'}$, where δ_{nm} is the Kronecker delta. Spherical harmonics are used to solve problems in spherical coordinates, such as analysing the thermal fluctuations of quasi-spherical vesicles.

1 P. M. Vlahovska and R. S. Gracia, *Phys. Rev. E*, 2007, **75**, 016313.
2 B. Kaoui, G. Biros and C. Misbah, *Phys. Rev. Lett.*, 2009, **103**, 188101.
3 V. V. Lebedev, K. S. Turitsyn and S. S. Vergeles, *Phys. Rev. Lett.*, 2007, **99**, 218101.
4 H. Zhao and E. S. G. Shaqfeh, *J. Fluid Mech.*, 2011, **674**, 578–604.
5 H. Zhao, A. P. Spann and E. S. G. Shaqfeh, *Phys. Fluids*, 2011, **23**, 121901.
6 H. Zhao and E. S. G. Shaqfeh, *J. Fluid Mech.*, 2013, **725**, 709–731.
7 T. Biben, A. Farutin and C. Misbah, *Phys. Rev. E*, 2011, **83**, 031921.
8 G. Ghigliotti, H. Selmi, L. El Asmi and C. Misbah, *Phys. Fluids*, 2012, **24**, 101901.
9 S. K. Veerapaneni, D. Gueyffier and D. Zorin, *J. Comput. Phys.*, 2009, **228**, 2334–2353.
10 Y. N. Young, S. Veerapaneni and M. J. Miksis, *J. Fluid Mech.*, 2014, **751**, 406–431.
11 D. Abreu, M. Levant, V. Steinberg and U. Seifert, *Adv. Colloid Interfac.*, 2014, **208**, 129–141.
12 M. A. Mader, V. Vitkova, M. Abkarian, A. Viallat and T. Podgorski, *Eur. Phys. J. E*, 2006, **19**, 389–397.
13 M. Levant and V. Steinberg, *Phys. Rev. Lett.*, 2012, **109**, 268103.
14 N. Callens, C. Minetti, G. Coupier, M. A. Mader, F. Dubois, C. Misbah and T. Podgorski, *Europhys. Lett.*, 2008, **83**, 24002.
15 V. Kantsler and V. Steinberg, *Phys. Rev. Lett.*, 2005, **95**, 258101.
16 V. Kantsler, E. Segre and V. Steinberg, *Phys. Rev. Lett.*, 2008, **101**, 048101.
17 V. Kantsler and V. Steinberg, *Phys. Rev. Lett.*, 2006, **96**, 036001.
18 M. Levant, J. Deschamps, E. Afik and V. Steinberg, *Phys. Rev. E*, 2012, **85**, 056306.
19 J. Deschamps, V. Kantsler, E. Segre and V. Steinberg, *Proc. Natl. Acad. Sci. U.S.A.*, 2009, **106**, 11444–11447.
20 J. Deschamps, V. Kantsler and V. Steinberg, *Phys. Rev. Lett.*, 2009, **102**, 118105.
21 A. P. Spann, H. Zhao and E. S. G. Shaqfeh, *Phys. Fluids*, 2014, **26**, 031902.
22 M. Abkarian, M. Faivre and A. Viallat, *Phys. Rev. Lett.*, 2007, **98**, 188302.
23 M. Abkarian and A. Viallat, *Soft Matter*, 2008, **4**, 653–657.
24 P. M. Vlahovska, T. Podgorski and C. Misbah, *C.R. Phys.*, 2009, **10**, 775–789.
25 P. M. Vlahovska, Y. N. Young, G. Danker and C. Misbah, *J. Fluid Mech.*, 2011, **678**, 221–247.
26 S. S. Lee, Y. Yim, K. H. Ahn and S. J. Lee, *Biomed. Microdevices*, 2009, **11**, 1021–1027.
27 L. A. Down, D. V. Papavassiliou and E. A. O'Rear, *Ann. Biomed. Eng.*, 2011, **39**, 1632–1642.
28 A. Sharma and U. S. Sharma, *Int. J. Pharm.*, 1997.
29 M. L. Immordino, F. Dosio and L. Cattel, *Int. J. Nanomed.*, 2006, **1**, 297–315.
30 Z. H. Huang, M. Abkarian and A. Viallat, *New J. Phys.*, 2011, **13**, 035026.
31 G. Boedec, M. Jaeger and M. Leonetti, *J. Fluid Mech.*, 2011, **690**, 227–261.
32 G. Boedec, M. Jaeger and M. Leonetti, *Phys. Rev. E*, 2013, **88**, 010702(R).
33 V. Kantsler, E. Segre and V. Steinberg, *Phys. Rev. Lett.*, 2007, **99**, 178102.
34 V. Narsimhan, A. P. Spann and E. S. G. Shaqfeh, *J. Fluid Mech.*, 2014, **750**, 144–190.
35 M. I. Angelova, S. Soléau, P. Méléard, F. Faucon and P. Bothorel, in *Trends in Colloid and Interface Science VI*, eds. C.

Helm, M. Losche and H. Mohwald, Steinkopff, 1992, pp. 127–131.

36 H. Raghuraman, S. Shrivastava and A. Chattopadhyay, *Biochim. Biophys. Acta, Biomembr.*, 2007, **1768**, 1258–1267.

37 M. Raffel, C. E. Willert, S. T. Wereley and J. Kompenhans, *Particle Image Velocimetry: A Practical Guide*, Springer-Verlag, 2nd edn. 2007.

38 J. G. Santiago, S. T. Wereley, C. D. Meinhart, D. J. Beebe and R. J. Adrian, *Exp. Fluids*, 1998, **25**, 316–319.

39 W. Thielicke and E. J. Stamhuis, *J. Open Res. Softw.*, 2014, **2**, e30.

40 J. Westerweel and F. Scarano, *Exp. Fluids*, 2005, **39**, 1096–1100.

41 J. R. Henriksen and J. H. Ipsen, *Eur. Phys. J. E*, 2002, **9**, 365–374.

42 P. Méléard, T. Pott, H. Bouvrais and J. H. Ipsen, *Eur. Phys. J. E*, 2011, **34**, 116.

43 W. T. Eadie, D. Drijard, F. E. James, M. Roos and B. Sadoulet, *Statistical methods in experimental physics*, North-Holland Publishing Company, 1971.

44 S. T. Milner and S. A. Safran, *Phys. Rev. A*, 1987, **36**, 4371–4379.

45 J. F. Faucon, M. D. Mitov, P. Méléard, I. Bivas and P. Bothorel, *J. Phys. France*, 1989, **50**, 2389–2414.

46 A. G. Ayuyan and F. S. Cohen, *Biophys. J.*, 2006, **91**, 2172–2183.

47 H. Bouvrais, T. Pott, L. A. Bagatolli, J. H. Ipsen and P. Méléard, *Biochim. Biophys. Acta, Biomembr.*, 2010, **1798**, 1333–1337.

48 D. Huster, P. Muller, K. Arnold and A. Herrmann, *Biophys. J.*, 2001, **80**, 822–831.

49 P. Shchelokovskyy, S. Tristram-Nagle and R. Dimova, *New J. Phys.*, 2011, **13**, 025004.

50 H. Bouvrais, P. Méléard, T. Pott, K. J. Jensen, J. Brask and J. H. Ipsen, *Biophys. Chem.*, 2008, **137**, 7–12.

51 J. F. Nagle, *Faraday Discuss.*, 2013, **161**, 11–29.

52 R. Dimova, *Adv. Colloid Interfac.*, 2014, **208**, 225–234.

53 R. S. Gracia, N. Bezlyepkina, R. L. Knorr, R. Lipowsky and R. Dimova, *Soft Matter*, 2010, **6**, 1472–1482.

54 V. Vitkova, J. Genova, M. D. Mitov and I. Bivas, *Mol. Cryst. Liq. Cryst.*, 2006, **449**, 95–106.

55 P. M. Bummer and G. Zografi, *Biophys. Chem.*, 1988, **30**, 173–183.

56 J. F. Nagle, M. S. Jablin, S. Tristram-Nagle and K. Akabori, *Chem. Phys. Lipids*, 2015, **185**, 3–10.

57 H. Zhao and E. S. G. Shaqfeh, *J. Fluid Mech.*, 2013, **719**, 345–361.

58 R. Bar-Ziv and E. Moses, *Phys. Rev. Lett.*, 1994, **73**, 1392–1395.

59 R. Bar-Ziv, E. Moses and P. Nelson, *Biophys. J.*, 1998, **75**, 294–320.

60 R. Lipowsky and H. G. Dobereiner, *Europhys. Lett.*, 1998, **43**, 219–225.

61 R. E. Goldstein, P. Nelson, T. Powers and U. Seifert, *J. Phys. II France*, 1996, **6**, 767–796.

62 G. Boedec, M. Jaeger and M. Leonetti, *J. Fluid Mech.*, 2014, **743**, 262–279.

63 T. R. Powers, *Rev. Mod. Phys.*, 2010, **82**, 1607–1631.

64 V. Narsimhan, A. P. Spann and E. S. G. Shaqfeh, *J. Fluid Mech.*, 2015, **777**, 1–26.

65 K. S. Chang and W. L. Olbricht, *J. Fluid Mech.*, 1993, **250**, 609–633.

66 C. de Loubens, J. Deschamps, M. Georgelin, A. Charrier, F. Edwards-Lévy and M. Leonetti, *Soft Matter*, 2014, **10**, 4561–4568.

67 C. de Loubens, J. Deschamps, G. Boedec and M. Leonetti, *J. Fluid Mech.*, 2015, **767**, R3.

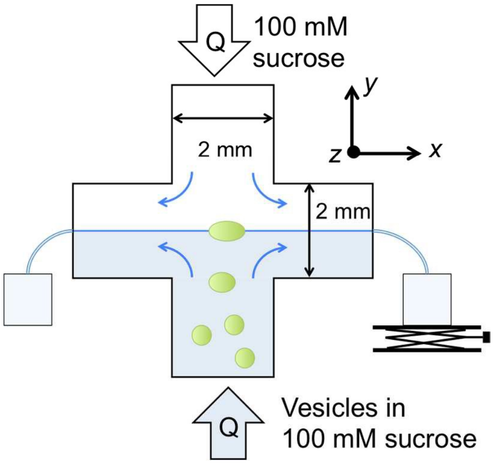

Figure 1 Microfluidic cross-slot device used to trap vesicles at the stagnation point of planar extensional flow. Adjusting the height of one outlet reservoir allowed for adjustment of the position of the vesicle along the outlet center streamline. All cross-slots are 2 mm wide. Devices had depths of 150, 158 and 383 µm.

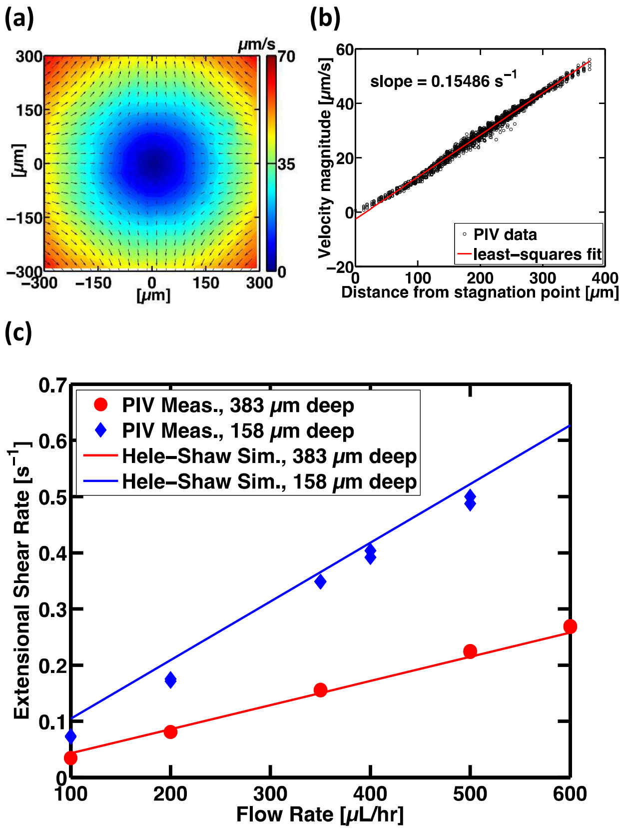

Figure 2 Particle Image Velocimetry (PIV) measurements in 2-mm-wide cross-slots. (a) The velocity field determined from the average of the correlation function in each interrogation area over 500 frames. Device depth 383 μm, flow rate 350 μL/hr. (b) The linear fit of the velocity magnitude as a function of distance to the stagnation point yields the measured extension rate near the stagnation point. The strongly linear behavior demonstrates that the flow within the cross-slot is indeed planar extensional flow. Device depth 383 μm, flow rate 350 μL/hr. (c) Comparison of PIV measurements with Hele-Shaw simulations for 2-mm-wide cross-slot devices of two depths. The uncertainties in the strain rate measurements are $\sigma_{\dot{\varepsilon}} \leq 0.0017$ s^{-1}.

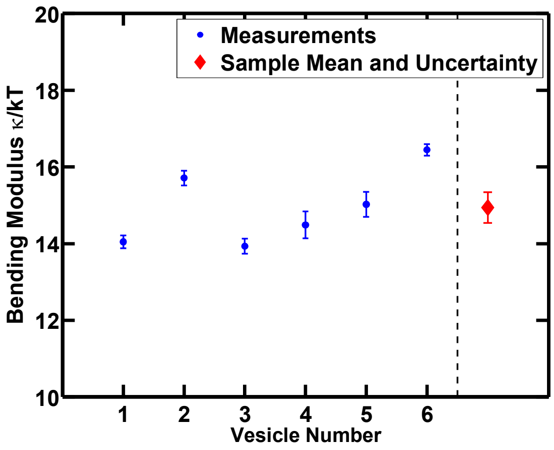

Figure 3 Bending modulus measurements for vesicles composed of DOPC and 15.8 mol% NBD PC. Individual vesicle measurements are shown to the left of the dashed line. To the right of the dashed line is the sample mean and its standard error ($\kappa = (14.94 \pm 0.40) \cdot kT$).

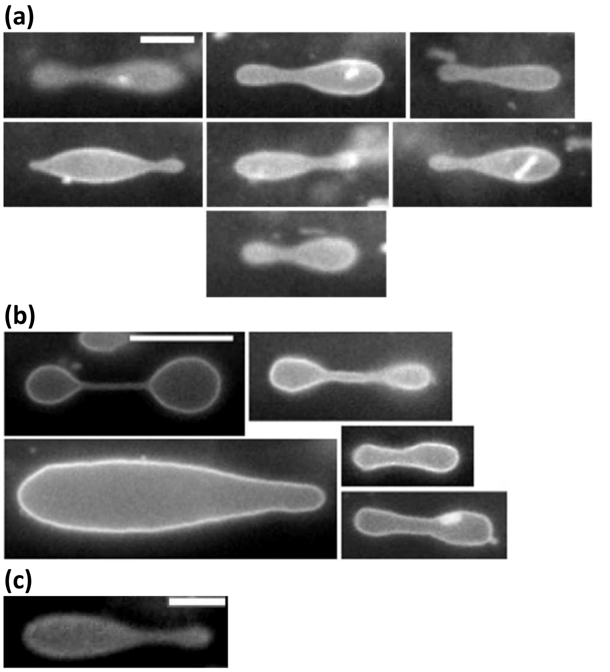

Figure 4 All unstable vesicles in planar extensional flow deform asymmetrically. (a) Early time point images for the seven unstable points in the stability diagram for which the entire instability evolution was observed (Figure 6, squares). Extensional strain rate $\dot{\varepsilon} = 0.368\ \mathrm{s}^{-1}$. (b) and (c): Other observations of the asymmetric shape instability at (b) 63x, $\dot{\varepsilon} = 0.353\ \mathrm{s}^{-1}$ and (c) 20x, $\dot{\varepsilon} = 0.368\ \mathrm{s}^{-1}$ that are included in the stability diagram but for which only one image was captured at short times (Figure 6, triangles). For these vesicles, there is less certainty in the reduced volume. Scale bars are 20 µm.

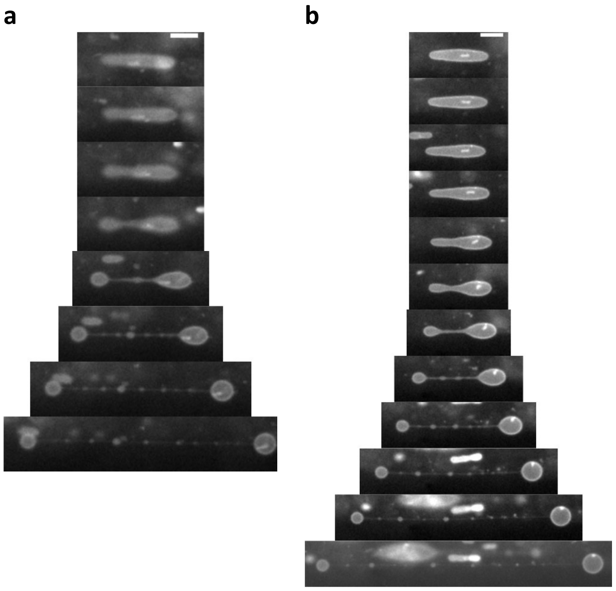

Figure 5 Time sequence of the asymmetric instability for two vesicles in planar extensional flow. Following the asymmetric burst phase, the tether elongates and undergoes pearling while the bulbous ends become more spherical. Extensional strain rate $\dot{\varepsilon} = 0.368\ \mathrm{s}^{-1}$, Scale bar is 20 µm. Time between frames is (a) 1.019 seconds and (b) 1.002 seconds.

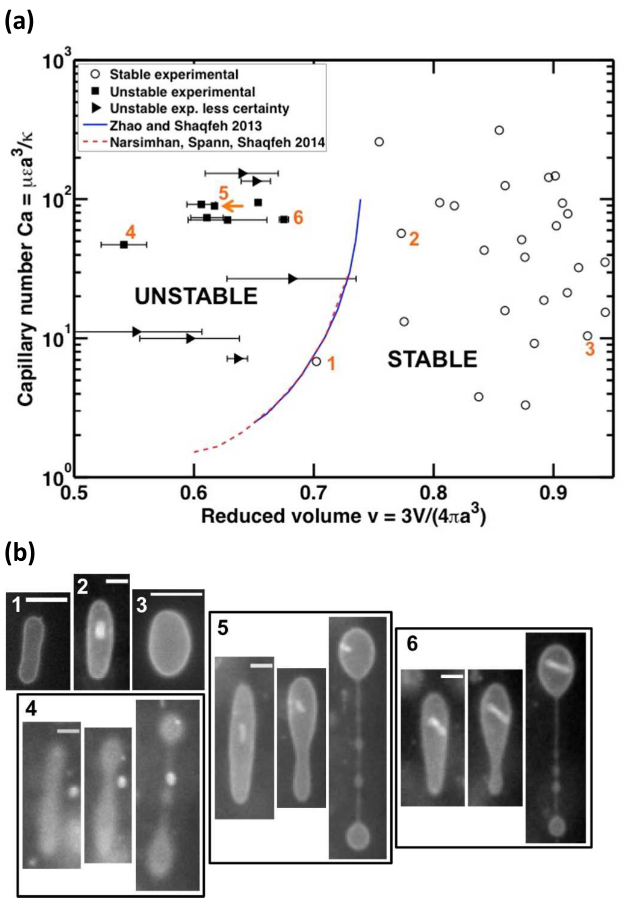

Figure 6 (a) Experimental stability diagram of individual vesicles in planar extensional flow. The experimental results are consistent with numerical predictions[34,57]. Squares: unstable vesicles for which we obtained sufficient images at short times to confidently assign the reduced volume. Triangles: unstable vesicles for which the reduced volume was estimated with less certainty from a single still image. Open circles: stable vesicles. Uncertainties in unstable vesicle reduced volumes are plotted. All other uncertainties are typically smaller than the data point markers. See Table S2 in the supporting information for all plotted point values and corresponding uncertainties. (b) Images of vesicle corresponding to the numbered points. Scale bars are 20 µm.

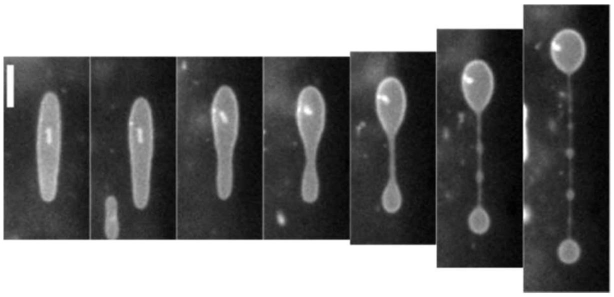

As asymmetric instability for vesicles undergoing extensional flow is confirmed via microfluidic experiments and bending modulus measurements.